International Forum on Aeroelasticity and Structural Dynamics
IFASD 2022
13-17 June 2022, Madrid, Spain

LOAD ALLEVIATION CAPABILITIES OF WINGS WITH NONLINEAR STRUCTURAL BEHAVIOR IN STATIONARY AND DYNAMIC LOAD CASES

Daniel Hahn[1], **Matthias Haupt**[1], **Sebastian Heimbs**[1]

[1]Cluster of Excellence SE^{2}A - Sustainable and Energy-Efficient Aviation
TU Braunschweig, D-38108 Braunschweig, Germany
and
Institute of Aircraft Design and Lightweight Structures, TU Braunschweig
Hermann-Blenk-Str. 35, D-38108 Braunschweig, Germany
daniel.hahn@tu-braunschweig.de

Keywords: passive load alleviation, nonlinear stiffness, coupled CFD-FEM-FSI

Abstract:

Coupled fluid-structure-interaction analyses of a concept for passive load alleviation based on structural nonlinearities are performed. The load alleviation concept is to include a component, which buckles at a critical load higher than cruise lift and subsequently allows the airfoil to deform and reduce lift. Different structural choices are analyzed. Load alleviation capabilities in stationary and dynamic gust load cases are observed. In dynamic cases the load alleviation capabilities are limited by mass inertia, when the gust encounter is of short duration.The present study employs Reynolds-Averaged-Navier-Stokes equations in the fluid model and compares the results with former results obtained from inviscid Euler simulation. Due to different pressure distribution and stronger nonlinear effects such as flow separation after shocks, the load alleviation capabilities of the structure are reduced compared to Euler in the more accurate RANS simulation, but are still present.

1 INTRODUCTION

The wing structural weight contributes significantly to the weight of an aircraft. Lighter aircraft allow for fuel and emission reduction. If the weight for one component is reduced, snowball effects allow for weight savings in other components as well. For example, a reduction of the gross weight due to wing weight reduction allows for smaller engines. This in turn lowers the gross weight and lift requirements, allowing again for smaller and lighter wings. Wing weight reduction thus contributes towards energy-efficient and environmentally friendly aviation. The wing weight depends on the amount of material needed to withstand the aerodynamic and internal loads. Lift is the largest load, as is equals the weight force of the aircraft in steady flight. The lift is distributed over the wing and contributes to the internal bending moment at the wing root. In maneuvers such as turns or vertical velocity changes, the lift exceeds the aircraft weight force by the load factor n_z. In turns with $30°$ bank angle, the load factor equals $n_z = 1.15$. For passenger comfort, changes in the vertical velocity like lift-off are performed with a similar load factor. However, the aircraft is required to sustain $n_z = 2.5$ in case it is aerodynamically possible to create that lift force. At high speed, high lift forces are produced already at low angles of attack. Since lift generation is aerodynamically limited by stall at high angles of attack, these high lifts can occur in cruise flight. Not only stationary maneuvers increase the load factor, also dynamic gust loads increase the wing load.

Load control or load alleviation aims to reduce the maximum loads which occur on the wing by shifting the lift distribution towards the wing root reducing the bending moment or reducing the overall possible load factor. Load alleviation techniques are divided into active and passive techniques. The current airliner generation uses deflections of the ailerons to lower the lift in the outer wing during high load cases [1]. New developments are towards improved actuation by fluidic [2] or piezoelectric actuators [3]. Implementing forward looking LIDAR sensors is investigated to improve the actuation control behavior [4].

The principle idea of passive load alleviation is to design the structure such, that high loads deform the structure in a lift reducing way. One way to achieve bending-twist coupling, which lowers the angle of attack in the outer wing and thus distributes the lift towards wing root, is aeroelastic tailoring [5]. Aeroelastic tailoring uses non-symmetrical stiffness distributions like specifically designed fiber composite layups [6] or skewed stiffeners [7]. It can not only be employed for load alleviation, but also cruise efficiency [8] and flutter suppression [9]. Alternative concepts are hinged wingtips [10] or a semi-passive method which uses temperature-dependent stiffness of components, which are electrically heated to the desired stiffness [11]. Dampening elements at the strut wing connection of strut braced wings can reduce dynamic gust loads [12].

Several investigated concepts for passive load alleviation utilize structural nonlinearities to create load alleviating deformation, which increases progressively with load. Such concepts are the implementation of multistable composite elements with snap-through behavior to suddenly change the stiffness distribution at a critical load [13, 14], negative stiffness spring devices for hinged wingtips [15] and box beam spars with buckling rear web to increase bending-twist coupling [16].

The present study originates from a project in the Cluster of Excellence SE^{2}A "*Sustainable and Energy-Efficient Aviation*", which aims at exploring such nonlinear concepts with high fidelity fluid structure interaction methods. The selected nonlinearity in this project is buckling. This is similar to bistable elements, but less sudden and there is no need to actuate the element to return into the original state. The authors of the present study demonstrated load alleviation capabilities of this concept in [17] using the inviscid Euler fluid model. The present study changes the fluid model to a viscid Reynolds-Averaged-Navier-Stokes (RANS) equation formulation. This formulation is more accurate and computationally expensive. Differences in the interaction behavior and load alleviation capabilities are shown and discussed. A resizing of the model is performed employing a parametric study with different design choices.

Section 2 describes the employed methods. The different structural designs are presented in section 3. Section 4 evaluates the designs in a quasi-stationary context and section 5 shows gust encounters with selected appropriate structural designs. Conclusions are given in section 6.

2 METHODS

The present study analyzes a quasi-2D section of a wing based on the SE^{2}A medium range reference configuration version 2 [18]. This configuration uses the DLR-F15 transonic airfoil [19]. The chord length of the 2D section is 2.3 m and it is extruded by 1 m. In a quasi 2D simulation the extrusion length has no influence on the results as no forces, displacements, or fluxes in that direction are considered. The simulation uses a partitioned approach with different software packages and models, which are described in this section.

2.1 Coupling environment

The central software of the analyses is the in-house coupling environment *ifls* [20]. It allows to couple different solvers and models for a partitioned multiphysics simulation. *Ifls* controls the solving process by generating updated input data for the individual solvers and starting the solution of one step. The resulting quantities like displacement, force, pressure, or temperature are interpolated to the grid of the second model and transferred as new boundary condition. The User defines the simulation process in the control code written in python. This code determines which and when quantities are transferred to which model, and when which solver is started to solve the next step. Iterations are set up using the control code. The communication between the control code and the third party solvers is done by a coprocess. Every solver to be used needs a solver-specific coprocess, because it defines, how input data is generated, a simulation step is started, and how resulting quantities are read. An advantage of this approach is, that a control code can be used with any solver, provided a coprocess for the solver is available.

2.2 Structural model

The calculation of the structural behavior is performed by the commercial finite element toolbox *Abaqus*. The model has 244 elements. Since the design of the structure is based on thin walled parts, the elements are shell elements. The design choices and variations are covered in more detail in section 3. Figure 1 shows the elements and coordinate directions. To make the model quasi 2D, only one element in the y-direction is used. The translation in y-direction and rotations around the z- and x-axes are locked for every node. Beam elements, which would make a real 2D model, are not used, because the coupling environment needs a coupling surface. The airfoil is fully fixed at the front spar and the leading edge. In aeroelastic simulations the interpolated aerodynamic forces are projected onto the nodes as concentrated forces. The *ifls* coprocess for *Abaqus* utilizes the *Abaqus Co-Simulation Engine* (CSE) as interface. In preliminary structural simulations without fluid response the pressure distribution in cruise is approximated by a polynomial regression of 5th degree, applied as pressure load and scaled linearly. Geometric nonlinearities are enabled, as the nonlinearities are the main topic of the study. The solver is set to an implicit dynamic scheme. This prevents convergence problems at the instabilities near the buckling load, also in quasi stationary calculations. The material model is an isotropic elastic material with an elastic modulus of 78 GPa and density of 2800 kg/m^3, corresponding to aluminum. The present study focuses on the fluid-structure interaction, so material plasticity and failure are not considered in this model.

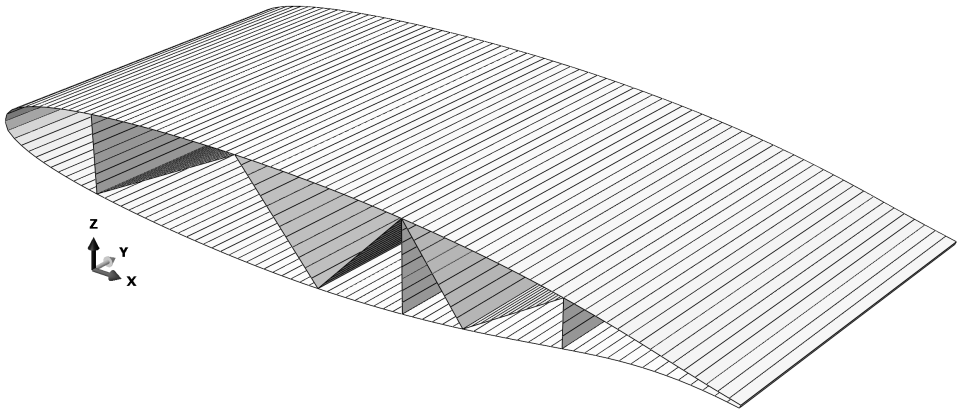

Figure 1: Structural model mesh and coordinate system.

2.3 Fluid model

The selected computational fluid dynamics solver is *DLR TAU-Code* [21]. The mesh and basic solver configuration are provided by a project partner [2]. The mesh has 700,000 cells. The area near the airfoil is highly refined, such that the boundary layer is resolved in high detail. Figure 2 shows the fluid mesh in the vicinity of the leading edge. The mesh is therefore well suited for calculations using the Reynolds-Averaged-Navier-Stokes (RANS) equations. In contrast to the Euler simulations used in the previous study [17], RANS equations take viscid effects like parasite drag and turbulence into account. The turbulence is not fully resolved like in a direct numerical simulation or a large eddy simulation. Instead, the effect of the turbulence is modeled as additional stress in the fluid. The Spallart-Almaras (SA) turbulence model is used.

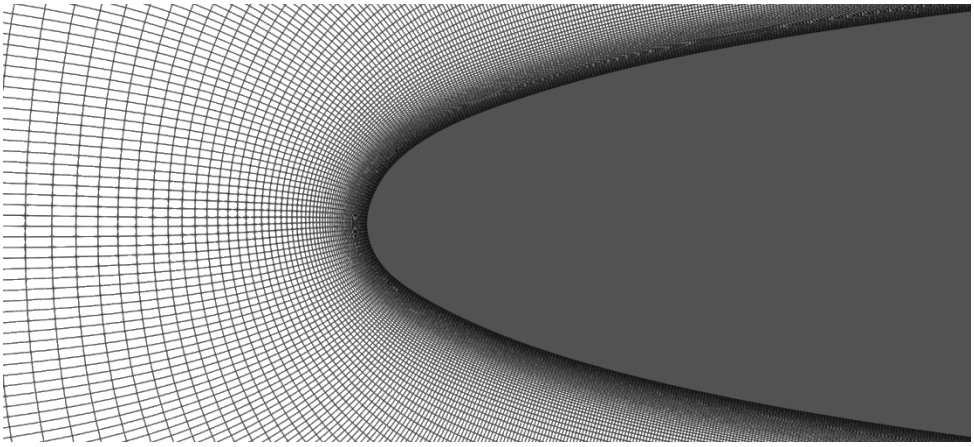

Figure 2: Fluid mesh at leading edge.

Unsteady terms are considered for calculations in the time domain. The atmospheric conditions are derived from the the cruise of the SE^{2}A medium range reference configuration version 2 [18]. The mach number and true airspeed are corrected for the wing sweep effect in the 2D simulation. Table 1 lists the cruise condition parameters. The angle of attack is set using *DLR TAU-Code's* rigid body motion tool. The deformed mesh is calculated by the deformation tool of *DLR TAU-Code*. Gusts are introduced into the simulation with the disturbance velocity approach included in *DLR Tau-Code*.

Table 1: Flight conditions in cruise

parameter	unit	value
altitude (ISA conditions)	m	10600
aircraft mass	kg	70640
mach number	-	0.78
corrected 2D mach number (sweep)	-	0.743
corrected 2D true airspeed (sweep)	m/s	220.5
lift coefficient	-	0.399

2.4 Aeroelastic analysis procedure

The analysis procedure is set up in the user-defined control code of *ifls*. It begins with a stationary fluid step to provide initial conditions. The time iteration loop starts subsequently. Each time step consists of a inner loop with two iterations. Before the inner loop is started, a structural predictor is formed taking the velocities and accelerations from the last time step into account. The inner loop starts with the calculation of the fluid on a deformed grid according to the predictor. The pressure forces are subsequently transferred to the structural model and the

deformation is calculated. To improve convergence, the resulting deformation is relaxed using Aitkin relaxation with the former predictor generating an updated deformation. This updated deformation is used as the predictor in the next inner iteration. By using inner iterations the coupling of fluid and structure is stronger than in a weak coupling, which would only transfer the quantities once per time step without feedback from the other model to the corrections. The time step length is set to 0.001 s in the present study.

This dynamic procedure in the time domain is also used for quasi stationary cases in the present study. The reason is the potentially unstable behavior of the structure, which can prevent convergence in a stationary structural simulation. In quasi stationary analysis a dynamic step response until up to 0.5 s is evaluated, allowing for comparison between the different structural designs. To improve the structural reaction time and come close to a steady state at 0.5 s the material density is reduced to 500 kg/m^3. This is feasible, because the dynamic history of the step response is not evaluated in the time domain. These step responses are evaluated for different angles of attack, corresponding to the lift coefficient C_L required for $n_z \in \{1.0, 1.2, 1.4, 1.8, 2.2, 2.4\}$ with the rigid airfoil. $n_z = 2.4$ is the lift developing at the angle attack produced by the highest vertical gust velocity defined in the certification specification CS25.341 [22]. The lift coefficient increment of the flexible structures is compared to the lift coefficient increment of a rigid reference airfoil.

3 STRUCTURAL DESIGNS

The structural concept is the same as in the previous study [17]. It is based on an internal stiffener, which buckles at the critical load. This reduces the shear stiffness of the airfoil. The trailing edge deforms upwards due to the lift forces. This motion reduces the effective angle of attack and hence reduces the generated lift. The concept is displayed in Figure 3 in the deformed and undeformed state.

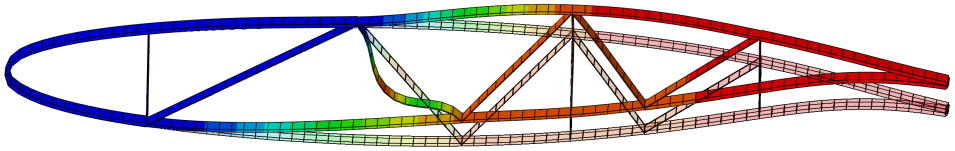

Figure 3: Load alleviation concept: Deformed structure above the critical load and original shape

Different structural choices are compared, starting with the resulting design from the previous study, referred to as Design A in the present study. New design choices are derived from the results of the calculations using RANS in the fluid model. These choices concern the thickness of the inner stiffeners t_i, the thickness of the outer skin t_o taking part in the shear deformation and the chord wise position of the buckling stiffener x_b. Table 2 summarizes the structural designs.

Some selected skin sections are 8 mm thick, which is a larger thickness than t_o. The reason is to provide stiffness in sections, which are not required to be deformed for the load alleviation technique. Especially the upper skin section between the front spar and the buckling stiffener must provide sufficient stiffness such that the buckling component is compressed instead of being lifted upwards due to skin bending. The trailing edge skin has also the larger thickness, since it does not contribute to the desired shear deformation.

Table 2: Structural Designs with inner thickness t_i, outer thickness t_o and chord-wise position of the buckling component x_b.

Design name	t_i, mm	t_o, mm	x_b, % chord
A	1.75	5	43
B	1.55	5	43
C	1.55	5	38
D	1.65	5	38
E	1.55	6	38
F	1.65	6	38

4 QUASI STATIONARY ANALYSES

In the quasi stationary analyses the step responses of the designs are evaluated regarding their load alleviation capabilities. Two objectives are considered. In the load cases for cruise $n_z = 1$ and maneuvering $n_z = 1.2$ the buckling component is not supposed to be in the postbuckling state. Small deformations of the airfoil and subsequent lift losses are allowed, because it is not possible with a flexible structure to achieve no deformation at all. Lift loss and deformation shall be small in these load states. The second objective considers the load cases with $n_z \geq 1.4$. In these load cases the deformation and lift reduction are supposed to be large, with the buckling component in the post buckled state.

4.1 Difference in Pressure Distributions between RANS and Euler

The structural design A successfully alleviated loads in the Euler calculations in [17]. This structure does not show load alleviation when using RANS. The stiffener supposed to buckle does not enter the postbuckling state in any of the load cases. This model is sized suiting to the load distribution resulting from the Euler calculation. As shown by Figure 4 for the load case of $n_z = 1.8$ with the rigid reference airfoil, the shock position is nearer to the leading edge when using RANS.

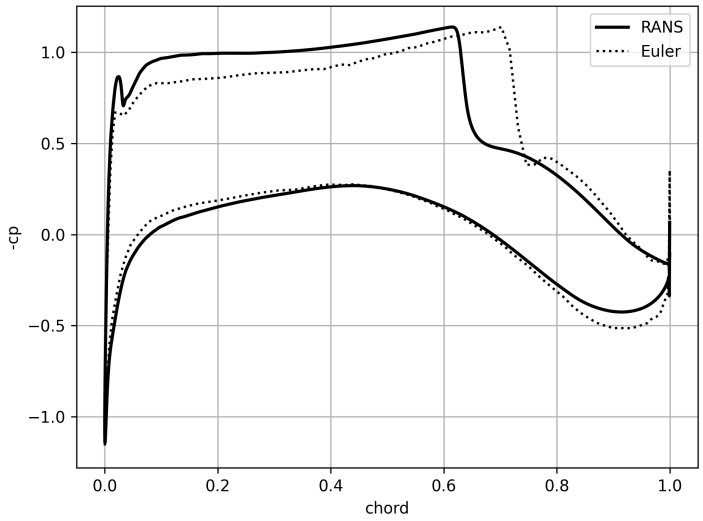

Figure 4: Pressure distributions at $n_z = 1.8$.

The structural concept relies on sufficient pitching moment by pressure differences towards the trailing edge to enter the postbuckling state of the buckling stiffener and to lift the rear part up. The shock shift towards the trailing edge results in less pitching moment at the buckling

stiffeners position. The stiffener sizing is sensitive to differences in the load distribution, as demonstrated by these results of design A. This result motivates the investigation of designs B, C, and D with reduced buckling stiffener thickness and forward shift of the buckling stiffener. Both measures are supposed to reach the critical load of the buckling stiffener at lower aerodynamic load. The forward shift additionally increases the flexible area of the airfoil potentially allowing for larger reductions of the effective angle of attack. Design B successfully sustains stiffness in cruise and alleviates load in high load scenarios. This is discussed in more detail in section 4.3. The difference in stiffener thickness between design A and design B is only 0.2 mm or 13 % and changes the behavior from no load alleviation to the desired behavior. This shows significant sensitivities to the sizing of the buckling component.

4.2 Stiffness requirements of the skin with forward shifted buckling component

The designs C and D are designs with a forward shifted buckling stiffener to increase the acting upward forces. Design C has the same inner structure thickness as design B. the inner structure thickness is increased in design D. Both designs fail to provide enough stiffness for the cruise condition. The stiffness of the inner structure in design C is not stiff enough, such that the buckling stiffener already buckles in cruise. Already at 0.2 s simulation time the lift coefficient C_L drops from 0.398 to 0.314. This drop is unfeasible and the series of load cases for design C, as well as the cruise case until 0.5 s is not continued. This result is not surprising, because the inner structure is sized suitable like Design B, which has less pitching moment acting on the buckling stiffener. Design D also has undesired deformation in cruise. Even though the stiffener is not in postbuckling mode, the trailing edge is lifted. The reason is a bulge in the upper skin between the middle spar and the buckling stiffener. Due to the larger area of this section the pressure forces lift it up, resulting lift of the trailing edge as well. The lift coefficient C_L drops from 0.398 to 0.359, which is still a significant reduction which is undesired. The bulge is additionally undesired because it reduces the airfoils performance. The deformations in cruise of designs C and D are displayed by Figure 5.

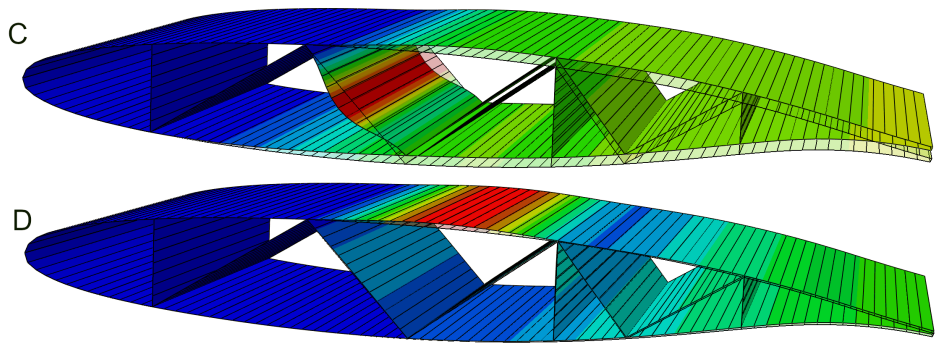

Figure 5: Undesired deformations in cruise with designs C and D.

A bulge in the upper skin like in Design D is also present in Design C before the buckling component buckles in the time history of the step response. This deformation may increase the tendency of the buckling stiffener to buckle at lower loads than intended. Since in both models the stiffness of the upper skin plays a major role in the undesired behavior, the designs E and F are introduced. These designs have an increased skin thickness to stabilize the tendency of the upper skin to form the observed bulge.

4.3 Comparison of stationary load alleviation between the designs

The increased skin thickness in designs E and F stabilizes the structure in cruise, such that the lift coefficient C_L does not drop lower than 0.371 in design E. The drop to 0.381 in design B is even lower than the corresponding drop to 0.378 in the Euler simulation of [17]. Structure F with 0.377 is very close to the Euler simulations. The buckling stiffener in Design E buckles already in cruise, however the remaining structure provides enough stiffness for the cruise load and shows only a small deformation of 6.2 mm of the trailing edge. In comparison, this deformation in Design C is already larger than 27 mm, when the simulation is stopped early at 0.2 mm. Design E therefore does not completely fulfill the cruise requirements, since the requirement of no buckled stiffener is violated, but since the requirement of no large lift loss is still fulfilled, the calculations with structure E are continued for comparison.

The resulting lift coefficients C_L of the flexible structures B, E, and F are shown together with the results of the rigid airfoil in Figure 6. The lift coefficients of the cases for $n_z = 1.8$ and $n_z = 2.2$ with designs B and E in this figure are averages of the last local maximum and minimum in the step response, because they show a remaining decaying oscillation from the step response at 0.5 s. This assumption is considered sufficient for the purpose of the present study, to evaluate the existing load alleviation potential and compare the potentials of the designs. All designs succeed to alleviate load in the load cases between $n_z = 1.4$ and $n_z = 2.2$. Design E fails to provide enough stiffness for $n_z = 1.2$, because the stiffener already buckled in cruise and the loss of stiffness leads to too large deformations in a load level, where this is not desired. The lift increment in this case is reduced by 54 % compared to the rigid airfoil. The lift increments are determined with respect to the cruise lift coefficient C_L of the corresponding flexible structure. The designs B and F provide enough stiffness at $n_z = 1.2$ to significantly increase the lift, which is required for maneuverability. In both cases, the lift increment is only reduced by 5 %. Design B shows the best behavior, because the nonlinearity above the critical load is strong and the lift is significantly reduced. The largest lift increment ΔC_L reduction with Design B is 68 % in the load case of $n_z = 1.8$ with angle of attack $\alpha = 1.4$. Due to the larger overall stiffness of design F, the nonlinearity is not is strong as in design B. The lift increments above the critical load are still significantly reduced, but the maximum reduction of 39 % is smaller than the reduction of 68 % in the same load case of structure B. These results show, that it is not beneficial to shift the buckling component towards leading edge in order to increase the pitching moment in this specific design concept. The reason is, that the skin area needs to be reinforced in order to prevent from too strong deformation already in the cruise case. If the buckling component is sized too weak the load alleviation behavior at high load cases is comparable to design B without the buckling component relocation, but the stability in cruise and normal maneuvers is reduced. In case the buckling component is sufficiently sized for cruise and maneuver flight, the overall stiffness reduces the load alleviation capabilities below the capabilities of structure B.

4.4 Behavior at high angles of attack

A significant difference of the results using RANS instead of Euler is small load alleviation at the load case with the highest angle of attack, which was determined using the maximum vertical gust velocity. In the Euler calculations of [17] the structure still reduces the lift increment ΔC_L by 96.6 % with a trailing edge deformation of 161 mm. The trailing edge deformation of design B using RANS does not exceed 70 mm. At this angle of attack there is already a large difference between the resulting lift coefficient C_L of the rigid airfoil. In the Euler simulations, C_L reaches 1.326. Using RANS the gradient of lift versus angle of attack $C_{L\alpha}$ decreases signif-

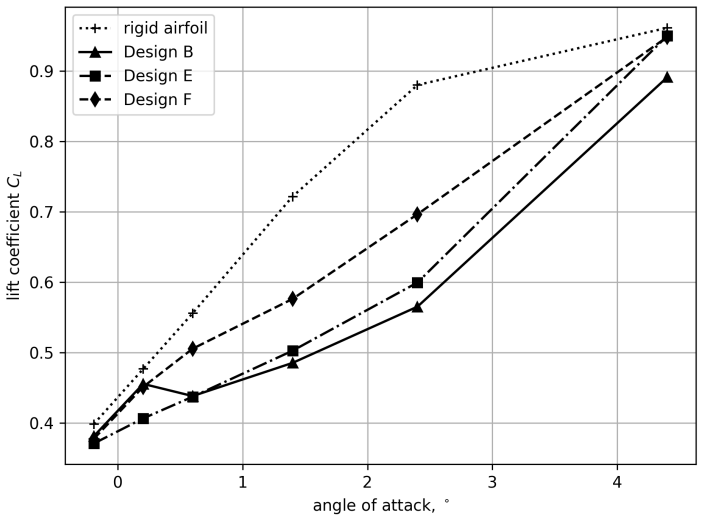

Figure 6: Lift coefficients at different angles of attack with flexible structures.

icantly after the load case of $n_z = 2.2$ due to separation. The lift coefficient C_L using RANS in the maximum vertical gust velocity load case is 0.961. Compared to Euler, this results in less total force on the airfoil and to less moment because the shock position is shifted forward in the RANS simulation. This limits the deformation of the airfoil compared to the Euler simulations. Additionally, the low $C_{L\alpha}$ reduces the influence of the effective angle of attack reduction on lift.

To analyze the flow at high angles of attack with a deformed structure, uncoupled aerodynamic simulations of the original rigid airfoil and a fixed deformed airfoil with trailing edge deformation of 50 mm are performed. The corresponding lift coefficients are plotted in Figure 7. It is visible, that the lift coefficients of the deformed airfoil do not approach the maximum lift linearly or slowly reduce the gradient like the clean airfoil. Instead, there is an increased rise from a state with significant load reduction to the maximum lift coefficients of the clean airfoil. The mach number contour insets show, that this nonlinear change happens, when two supersonic areas merge to one larger supersonic area. From this point on, the deformed structure is able to produce similar lift coefficients compared to the non deformed counterpart.

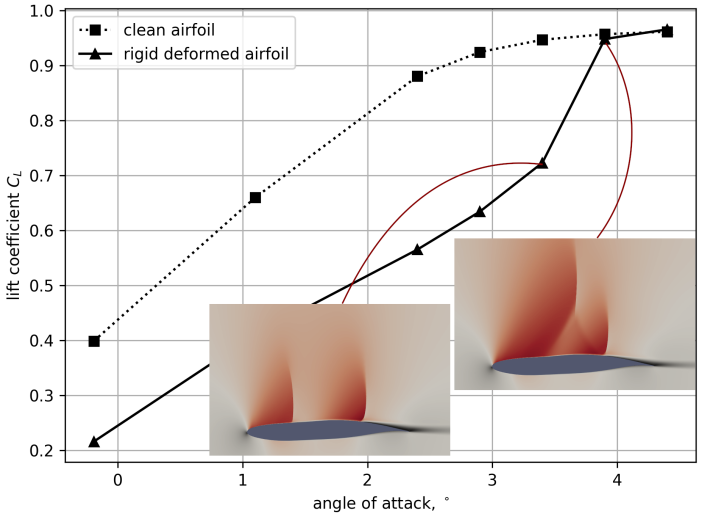

Figure 7: Lift coefficients and mach number contour at different angles of attack with a rigid deformed structure.

These results show that the load alleviation potential in high angle of attack scenarios in transonic cruise is limited by the nonlinear aerodynamics in transonic flight, which allows the deformed structure to eventually reach the same lift coefficient as the undeformed structure.

5 DYNAMIC GUST LOAD ANALYSES

For the investigation of the dynamic gust load alleviation capabilities, four 1-cosine gusts out of the spectrum defined in certification specification CS25.341 are selected. The vertical gust velocities depend on the properties of the aircraft and gust length and are calculated for the SE^2A medium range reference configuration version 2. The gust spectrum starts with a short 18 m gust with 11.97 m/s vertical velocity and ends with a 214 m long gust with a vertical velocity of 18.06 m/s. The selected intermediate gusts are 36 m and 108 m long and have vertical velocities of 13.45 m/s and 16,15 m/s. These gusts are encountered with a true airspeed of 220.5 m/s after 0.1 s simulated time. The time history of the vertical velocities at the leading edge is shown by Figure 8. The same vertical velocity acts on the trailing edge 0.01 s later.

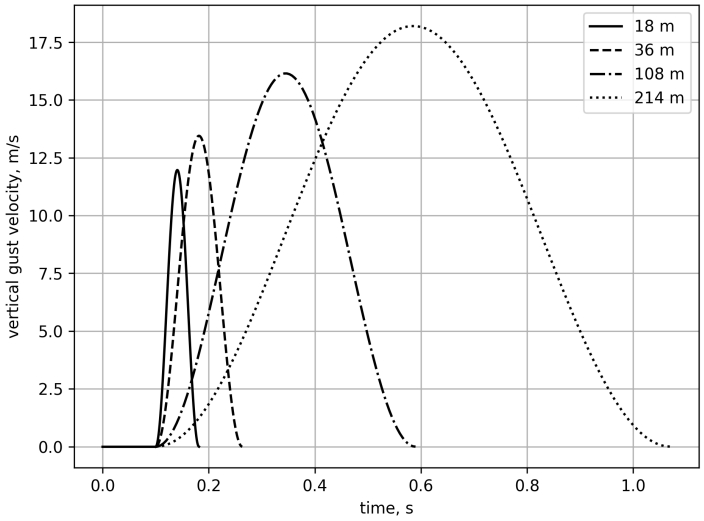

Figure 8: vertical gust velocities in the time domain at the leading edge with 220.5 m/s airspeed.

5.1 Reference rigid airfoil

Figure 9 shows the resulting lift coefficients during the gust encounters for the rigid airfoil. Results from both RANS and Euler calculations are shown. Like in the stationary case, it is visible, that the maximum lift coefficient in the RANS simulations is limited by the nonlinear transonic effects compared to the Euler simulations. This is most significant in the longest 214 m gust. It is also noticeable, that the lift coefficient starts to slightly decrease before the maximum vertical velocity is reached, whereas in the Euler simulations, the peak lift coefficient occurs shortly after the maximum vertical velocity.

5.2 Gust encounters of the flexible structure

The resulting lift coefficients C_L for the flexible structures of design B, E, and F are given in Figure 10. The plot starts at 0.08 s simulated time, when the flexible structures already reached the cruise state with slightly reduced C_L compared to the rigid airfoil. The gust encounter starts at 0.1 s simulated time. In the shortest gust, the lift is not significantly reduced, like in the results of the Euler simulations in [17]. The first reason is the short encounter duration, which does not allow the inert mass to deform, before the gust leaves the airfoil. A second reason is the low C_L reached in the rigid airfoil compared to the long gusts. This reduces the forces acting

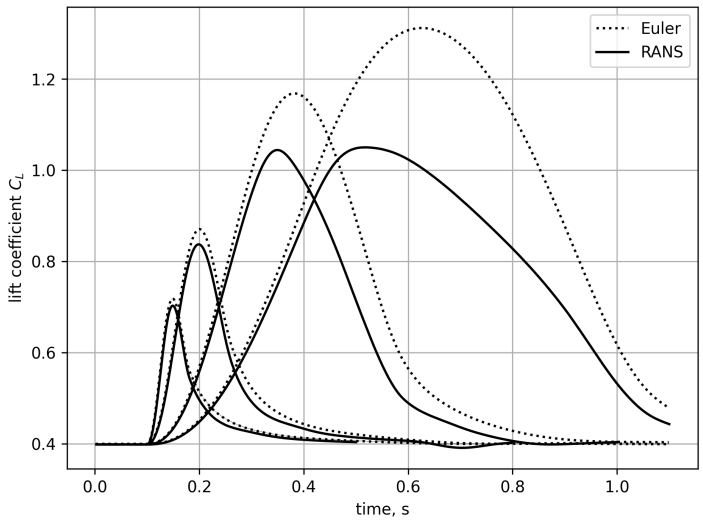

Figure 9: Lift coefficients during gust encounter with the rigid airfoil.

on the airfoil, which reduced the deformation rate even further. Even though the critical load is reached and the buckling stiffener enters postbuckling mode during the encounter, the trailing edge does not significantly move upwards. The longer gusts provide more time for the inert mass to deform, such that in the longer gusts a reduction of the lift increment ΔC_L is observed for all analyzed designs.

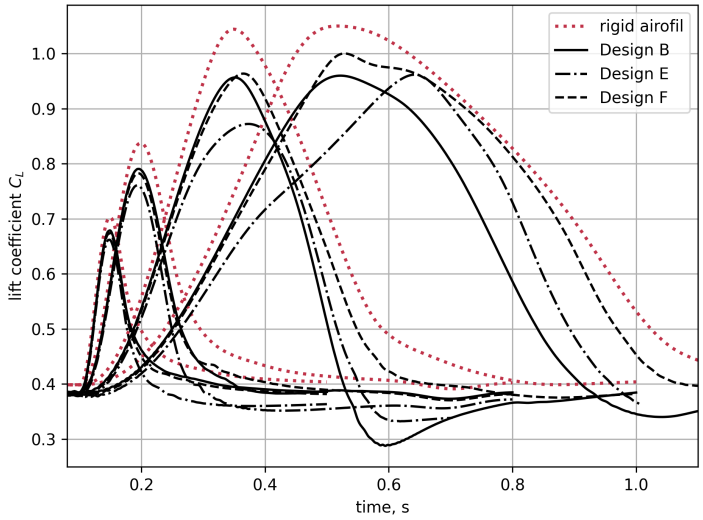

Figure 10: Lift coefficients during gust encounter with the flexible structures.

In comparison between the designs, design E alleviates the most lift in the 36 m and 108 m gust. The longest 214 m gust is best alleviated by design B. Design F shows the worst performance of the designs, which corresponds to the quasi stationary results. The difference between structure B and F is small compared to the quasi stationary results and most pronounced in the longest gust. In the shorter gusts, inertia seems to influence the lift reduction more than the stiffness distribution advantages of structure B found in the quasi stationary analyzes. In the longer gust the influence of the inertia decreases due to the longer time for the structure to react. In this case design B has significantly better load alleviation capabilities of 11.1 % ΔC_L reduction compared to design F with 4.4 %. Design E has the largest ΔC_L reduction also in beginning phase of the 214 m gust. After 0.4 s the lift increase shows a kink. In this position the deformation

starts to slow down because of the alleviated load. Due to the vertical velocity still increasing until 0.58 s the lift continues to rise, even higher than with design B to a ΔC_L reduction of 9.3 %. The pressure distribution changes from a state with two supersonic areas to the combined supersonic field between 0.4 s and 0.6 s, similar to the insets of Figure 7 in the quasi stationary simulations. In the shorter gusts and the other structures the deformation does not happen fast enough to build a pronounced state with two supersonic areas before the peak C_L. When the deformation reaches the shape, which produces this distribution, the vertical velocity is already large, such that the supersonic areas connect. The difference in reaction time allows design E to alleviate significantly more lift in the 108 m gust compared to design B. Design E reduces the lift increment by 22.4 % in this gust, whereas design B reduces the lift increment by 10.9 %.

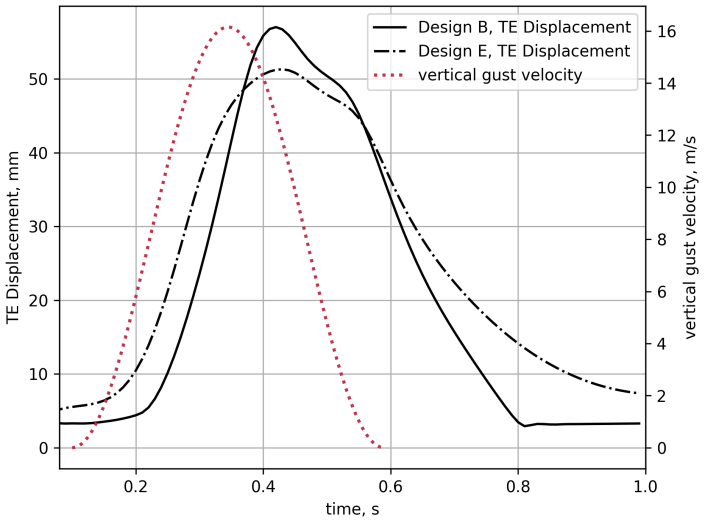

Figure 11: Trailing edge (TE) deformations and vertical velocity in the 108 m gust

The reduced reaction time of design E is well seen in Figure 11. The structure starts to significantly deform at lower gust velocities than in design B. The reason is, that structure E is already in a postbuckled state in cruise, even though the deformation at cruise load is quite small. As discussed in section 4.3 design B does not deform significantly at $n_z = 1.2$, whereas structure E does. This results in the earlier reaction time of the structure with design E, because it starts to deform with any increased lift, whereas structure B needs the critical lift to start buckling and deform. The difference in reaction time results in a large difference in peak lift. At the lift peak time of 0.35 s, the deformation of design E is still larger than the deformation of design B. Thereafter, the deformation of design B exceeds the deformation of design E, because of the larger remaining lift. The maximum deformation is reached, when the gust is already decreasing, such that it has no effect on the maximum lift coefficient.

The disadvantages in the stationary behavior of design E are thus advantageous for dynamic gust load cases. Since the lift in the stationary behavior keeps increasing with increasing angle of attack, an airplane with design E would still be able to perform maneuvers, but the required angle of attack is larger and the deformation is present, resulting in decreased aerodynamic performance even in very gentle maneuvers. Design B, which has the preferred stationary behavior, is still able to reduce the gust loads. It is therefore the most successful design in the present study.

6 CONCLUSIONS

This paper presents aeroelastic analyzes of a passive load alleviation technique based on structural nonlinearities. A stiffener is sized to buckle at a critical lift above cruise lift to change the airfoil stiffness and allow the airfoil to change camber in order to alleviate load. It extends the former study [17] by using Reynolds-Averaged-Navier-Stokes (RANS) equations instead of inviscid Euler equations in the fluid model. Compared to the Euler analyzes the achieved lift increment ΔC_L reductions are smaller, when using RANS. Reasons are found to be differences in the pressure distribution resulting in less moment to move the deformable part of the airfoil, and the nonlinear aerodynamic behavior in the transonic regime at high loads. Compared to Euler, the maximum lift coefficients are reduced as separations form behind shock position. This limitation of maximum lift has effects on the load alleviation capabilities. Less lift produces less force to deform the airfoil into the load alleviation state. At high angles of attack the deformed structure produces the same lift as the undeformed, because the deformed structure approaches the lift limit aswell.

Load alleviation is demonstrated for stationary and dynamic gust load cases comparing different structural design choices. The most successful design in the present study achieves 67 % lift increment reduction in the best stationary case of an angle of attack producing $n_z = 1.8$ for the rigid airfoil. It does not reduce the load significantly below $n_z = 1.2$, which is desired for maneuvering. In the best dynamic case of a long gust, it achieves 11.1 % lift increment reduction. Generally, a high sensitivity of the behavior to design choices is found. Competing designs with an increased lever area do not perform as well, because the stiffness of the surrounding skin needs to be increased in order to maintain lift in cruise. In dynamic simulations a design, which is already in a postbuckled state at cruise but still produces enough cruise lift, has advantages because of faster reaction time. The reaction time is a significant limitation of the load alleviation capabilities in dynamic gust loads, because the gust may have already passed the airfoil, when it starts to move significantly. The design with fast reaction time is not well suited for stationary maneuver flight, since small lift increments are already alleviated due to the early onset of significant deformation.

Due to the differences between RANS and Euler results, the analysis and design of structures employing the concept of nonlinear stiffness should take RANS into account. As the present study is focused on the interaction behavior of fluid and structure, material plasticity and failure is not considered. Revisions of material properties or the structural design my be necessary in practical applications.

Future work will extend this 2D design to a 3D wing, which allows to also consider wing twist. A previous study developed a structural concept for nonlinear bending-twist coupling [23] to be used in the 3D wing.

ACKNOWLEDGMENTS

We would like to acknowledge the funding by the Deutsche Forschungsgemeinschaft (DFG, German Research Foundation) under Germany's Excellence Strategy **EXC 2163/1** - Sustainable and Energy Efficient Aviation - **Project ID 390881007**.

7 REFERENCES

[1] Regan, C. D. and Jutte, C. V. (2012). Survey of Applications of Active Control Technology for Gust Alleviation and New Challenges for Lighter-weight Aircraft. Accessed 03.08.2020.

[2] Asaro, S., Khalil, K., and Bauknecht, A. (2021). Unsteady Characterization of Fluidic Flow Control Devices for Gust Load Alleviation. In A. Dillmann, G. Heller, E. Krämer, and C. Wagner (Eds.), *New Results in Numerical and Experimental Fluid Mechanics XIII*, vol. 151 of *Notes on Numerical Fluid Mechanics and Multidisciplinary Design*. Cham: Springer International Publishing, pp. 153–163. doi:10.1007/978-3-030-79561-0_15.

[3] Henry, A. C., Molinari, G., Rivas-Padilla, J. R., et al. (2019). Smart Morphing Wing: Optimization of Distributed Piezoelectric Actuation. *J. Intell. Mater. Syst. Struct.*, 57(6), 2384–2393. doi:10.2514/1.J057254.

[4] Fezans, N. and Joos, H.-D. (2017). Combined Feedback and LIDAR-Based Feedforward Active Load Alleviation. In *AIAA Atmospheric Flight Mechanics Conference*. Grapevine, Texas: American Institute of Aeronautics and Astronautics. doi:10.2514/6.2017-3548.

[5] Shirk, M. H., Hertz, T. J., and Weisshaar, T. A. (1986). Aeroelastic tailoring - Theory, practice, and promise. *Journal of Aircraft*, 23(1), 6–18. doi:10.2514/3.45260.

[6] Krüger, W. R., Dillinger, J., de Breuker, R., et al. (2019). Investigations of passive wing technologies for load reduction. *CEAS Aeronautical Journal*, 10(4), 977–993. doi:10.1007/s13272-019-00393-2.

[7] Abdelkader, A., Harmin, M., Cooper, J., et al. (2011). Aeroelastic Tailoring of Metallic Wing Structures. In *52nd AIAA/ASME/ASCE/AHS/ASC Structures, Structural Dynamics and Materials Conference*. Denver, Colorado: American Institute of Aeronautics and Astronautics. doi:10.2514/6.2011-1712.

[8] Thuwis, G. A. A., de Breuker, R., Abdalla, M. M., et al. (2010). Aeroelastic tailoring using lamination parameters. *Structural and Multidisciplinary Optimization*, 41(4), 637–646. doi:10.1007/s00158-009-0437-6.

[9] Bendiksen, O. O. (1988). Recent Developments in Flutter Suppression Techniques for Turbomachinery Rotors. *Journal of Propulsion and Power*, 4(2), 164–171. doi:10.2514/3.51283.

[10] Castrichini, A., Hodigere Siddaramaiah, V., Calderon, D., et al. (2015). Nonlinear folding wing-tips for gust loads alleviation. In *56th AIAA/ASCE/AHS/ASC Structures, Structural Dynamics, and Materials Conference*. Kissimmee, Florida. doi:10.2514/6.2015-1846.

[11] Raither, W., Heymanns, M., Bergamini, A., et al. (2013). Morphing wing structure with controllable twist based on adaptive bending-twist coupling. *Smart Materials and Structures*, 22(6), 065017. doi:10.1088/0964-1726/22/6/065017.

[12] Szczyglowski, C. P., Neild, S. A., Titurus, B., et al. (2017). Passive gust loads alleviation in a truss-braced wing using integrated dampers. In *International Forum on Aeroelasticity and Structural Dynamics, IFASD*. Como, Italy.

[13] Arrieta, A. F., Kuder, I. K., Rist, M., et al. (2014). Passive load alleviation aerofoil concept with variable stiffness multi-stable composites. *Composite Structures*, 116, 235 – 242. doi:10.1016/j.compstruct.2014.05.016.

[14] Cavens, W. D. K., Chopra, A., and Arrieta, A. F. (2021). Passive load alleviation on wind turbine blades from aeroelastically driven selectively compliant morphing. *Wind Energy*, 24(1), 24–38. doi:10.1002/we.2555.

[15] Castrichini, A., Cooper, J. E., Wilson, T., et al. (2016). Nonlinear negative stiffness wingtip spring device for gust loads alleviation. In *AIAA 15th Dynamics Specialists Conference*. San Diego, California. doi:10.2514/6.2016-1574.

[16] Runkel, F., Fasel, U., Molinari, G., et al. (2018). Wing twisting by elastic instability: A purely passive approach. *Composite Structures*, 206, 750 – 761. doi: 10.1016/j.compstruct.2018.07.095.

[17] Hahn, D., Haupt, M., and Heimbs, S. (2022). Passive Load Alleviation by Nonlinear Stiffness of Airfoil Structures. In *AIAA SCITECH 2022 Forum*. San Diego, California: American Institute of Aeronautics and Astronautics. doi:10.2514/6.2022-0318.

[18] Karpuk, S. and Elham, A. (2021). Conceptual Design Trade Study for an Energy-Efficient Mid-Range Aircraft with Novel Technologies. In *AIAA Aerospace Sciences Meeting 2021*. Online Event.

[19] Wild, J. (2013). Mach and Reynolds Number Dependencies of the Stall Behavior of High-Lift Wing-Sections. *Journal of Aircraft*, 50(4), 1202–1216. doi:10.2514/1.C032138.

[20] Haupt, M., Nies, R., Unger, R., et al. (2006). Computational aero-structural coupling for hypersonic applications. In *9th AIAA/ASME Joint Thermophysics and Heat Transfer Conference*. San Francisco, California. doi:10.2514/6.2006-3252.

[21] Schwamborn, D., Gerhold, T., and Heinrich, R. (2006). The DLR TAU-code: Recent applications in research and industry. In *European Conference on Computational Fluid Dynamis ECCOMAS CFD*. Egmond aan Zee, The Netherlands.

[22] EASA (2020). Certification Specifcations CS25 Amendment 17. Accessed 04.12.2020.

[23] Hahn, D. and Haupt, M. (2020). Potential of the nonlinear structural behavior of wing design components for passive load alleviation. In *Deutscher Luft- und Raumfahrtkongress, DLRK*. Online Event. Submitted for publication in CEAS Aeronautical Journal.

COPYRIGHT STATEMENT